EFFECT OF COARSE CARBIDE PARTICLE on SR embrittlement in the HAZ of 2 1/4Cr-1Mo steel

H. Kawakami, K. Tamaki, J. Suzuki, K. Takahashi, Y. Imae and S. Ogusu.

ABSTRACT

The authors pointed out that growth of the carbide particle is related to SR embrittlement in the HAZ of 2 1/4Cr-1Mo steel in a previous study. Suitable image processing was employed to evaluate the shape of a large number of carbide particles in a SEM image. An image-dividing technique was needed in for the difference of tone in each area of a SEM image. Image processing included image dividing, brightness and contrast, as well as a contraction and smoothing operation. The shape of the particle changed from the sphere type to the needle or polygon type because of the progress of SR treatment. The change of aspect ratio of the particle in the cross-section has a good correlation with the increment of SR treatment time. However, the aspect ratio of the particles on the fracture surface did not correspond with that of the cross-section in the long time range. This was confirmed by SEM observation on a pair of fracture surfaces, where coarse carbide particles were broken into pieces. Coarse carbide particle may accelerate SR embrittlement by acting as a path for crack propagation and a crack initiation site for brittle fracture. The type of carbide particles was investigated by X-ray diffraction. M_2C (Mo_2C type), M_7C_3 (Cr_7C_3 type) and $M_{23}C_6$ ($Cr_{23}C_6$ type) carbides were identified in the time range of SR embrittlement. The coarse carbide observed when SR embrittlement occurred significantly was confirmed as $M_{23}C_6$ type by TEM observation. The calculation results based on the Eshelby theory show that the change of shape of the carbide particle can affect crack propagation of brittle fracture.

IIW-Thesaurus keywords: Carbides; Embrittlement; Heat affected zone; Imaging; Steels.

1 Introduction

The four types of temper embrittlement appear in the HAZ of 2 1/4Cr-1Mo steel. Temper embrittlement disappears by stress relief annealing (SR treatment) [1]. However, SR embrittlement appears in the long-time range of SR treatment [2], also as a result of the time range growth of the carbide particle [3]. Large-scale measurement is required to evaluate the action of coarsened carbide particles on SR treatment because a number of particles exist in a small area. Image processing is an effective technique for systematic investigation of the shape of the carbide particle. Behaviour of growth of the carbide particle was investigated by the assembled image processing technique fitted for the carbide particle in a SEM image. Diameter and aspect ratio of the carbide particle observed on the cross-section area and the fracture surface were measured as the shape parameters in this study. Coarsened carbide on the cleavage fracture surface was broken down into individual pieces by comparison with each shape parameter. Identification of coarse carbide was carried out by X-ray diffraction and TEM observation. The effect of coarse carbide on SR treatment was evaluated by numerical calculation.

2 Experimental system

2.1 Specimen

The chemical composition of 2 1/4Cr-1Mo steel is shown in Table 1. The microstructure of the HAZ was reproduced by a weld-thermal cycle simulator. The synthetic HAZ specimen was produced by thermal history, with a heating rate of 92 K/s, with the ultimate temperature of 1 623 K and cooling rate of 21 K/s. The synthetic HAZ specimen was tempered at 975 K directly. Temper embrittlement was detected by the transition temperature of Charpy impact test in a previous study [3, 4]. The specimen with brittle fracture mode at the test temperature below 140 K was used for observation of the carbide particle in this study.

Table 1 – Chemical composition of 2 1/4Cr-1Mo steel [Mass %]

C	Si	Mn	P	S	Cr	Mo	Cu	N	Al_{sol}
0.14	0.16	0.56	0.006	0.002	2.17	0.90	0.01	0.0032	0.017

Doc. IIW-2052-09, recommended for publication by Commission IX "Behaviour of Metals Subjected to Welding."

2.2 Image processing

The cross-section and the fracture surface of the specimen were etched by nital to observe the carbide particles. The carbide appears as a white particle in a SEM image. Figure 1 shows the flow chart of the assembled image processing to detect the shape of white carbide particles. Image dividing is executed to select a suitable value of brightness and contrast treatment for each particle with a different grey scale [Figures 1 a), b)]. Each divided image was gathered again by image alignment [Figure 1 c)]. Addition and removing of a one pixel layer at the outside of the particle were operated to obtain the smooth edge by contraction and CE smoothing [Figures 1 d), e)]. Diameter and aspect ratio were measured for the carbide particle in a final binary image [Figure 1 e)]. The schematic diagram of each diameter of the major and minor axes of the particle is shown in Figure 2. The aspect ratio D/D' was calculated as a ratio of diameter of the major to minor axes. Figure 3 a) shows an example of an SEM image, including many fine carbide particles. The relation between the area of the carbide particle between visual measurement and image processing is shown in Figure 3 b). The area examined with image processing corresponded with that conducted by visual measurement.

3 Experimental results

3.1 Relationship between SR embrittlement and growth of carbide [3]

SR embrittlement was detected by an increment of the transition temperature vTr_{30}. The de-embrittled state occurred by suitable SR treatment at 975 K for 5 h as shown in Figure 4 a). The transition temperature rose gradually with the duration of SSR. The average size of the carbide particle increased similarly as shown in Figure 4 b). The density of carbide observed on the cross-section area and the fracture surface are shown in Figure 4 c). The number of carbides on the fracture surface was larger than that of the cross-section area and always from the SSR. These results suggest that coarsened carbide may promote SR

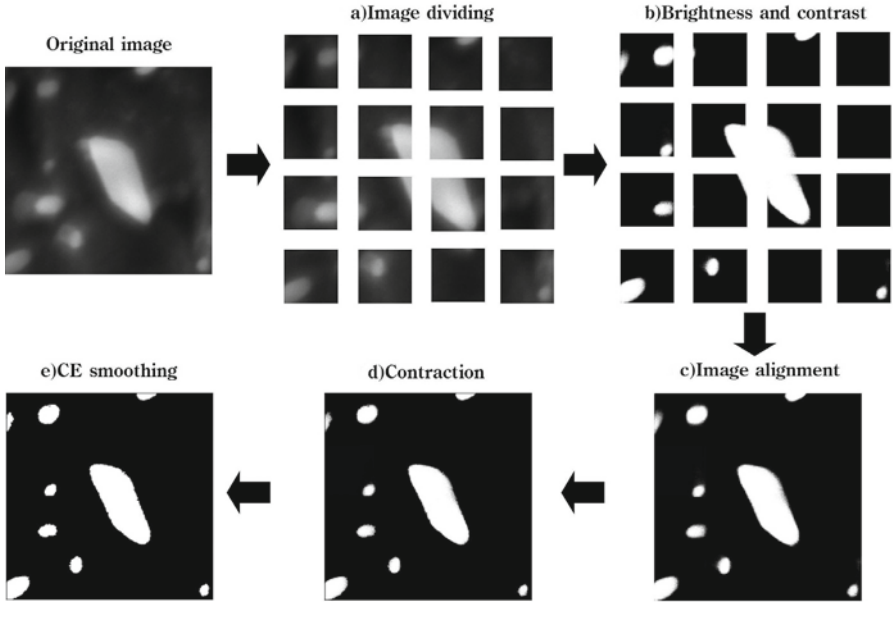

Figure 1 – Flow chart of image processing for carbide particle in an SEM image

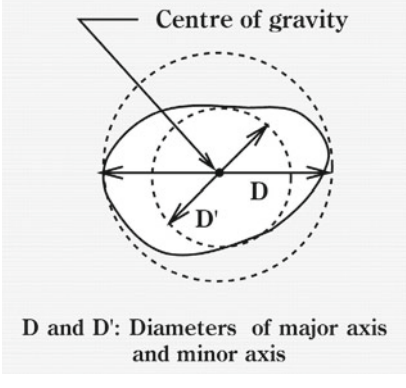

Figure 2 – Schematic diagram for diameters of major and minor axes

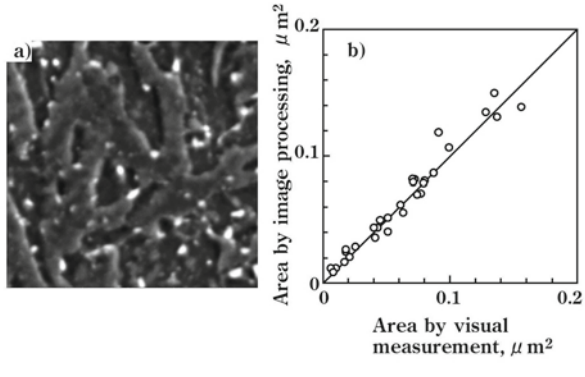

Figure 3 – An SEM image with fine carbide particles and the relation between the area of particle and image processing and visual measurement

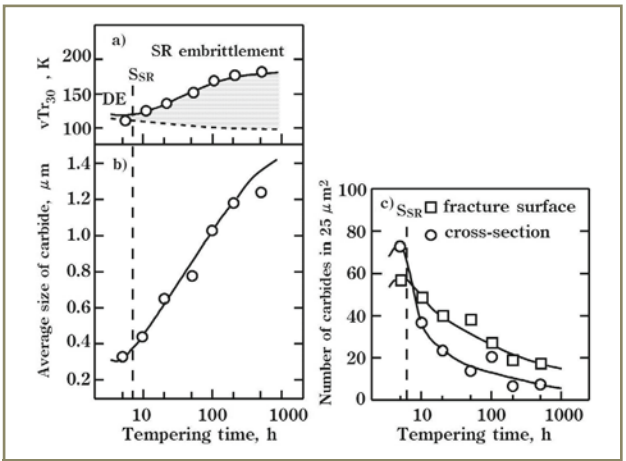

Figure 4 – Detection of SR embrittlement and behaviour of growth of carbide particles during the time frame of SR treatment

embrittlement by the crack propagation along the carbide/matrix boundary or into the carbide.

3.2 Behaviour of growth of carbide

The distribution of diameter of the major axis is shown in Figure 5. The significant peak existed as a result of distribution in the initial stage of SR embrittlement [Figures 5 a) to c)]. The average diameter of the major axis increased in the middle stage. Smoothing of distribution was confirmed instead of the translation of the peak observed in the initial stage [Figures 5 d), e)]. The increment of the average diameter continued over a long time range, but the position of maximum frequency in distribution was maintained [Figures 5 f), g)]. This result suggests that one of the mechanisms for growth of the carbide may be preferential growth of some of the carbides at the expense of others. The average diameter of the carbide on the fracture surface was larger than that of the cross-section area [Figures 5 h) to n)]. However, the particle with maximum diameter in the cross-section area could not be observed on the fracture surface over a long time range when SR embrittlement occurred significantly [Figures 5 m), n)]. This result suggests that coarse carbides may be broken during crack propagation.

The comparison between the cross-section and the fracture surface by the relationship between aspect ratio D/D' and diameter of the major axis D is shown in Figure 6. The particle with an aspect ratio of 1 is spherical in shape. Fine spherical carbide particles were observed mainly at the tempering time of 5 h when the de-embrittled state occurs [Figure 6 a)]. The shape of the particle on the fracture surface corresponds with that of the cross-section area [Figure 6 a')]. The crack may propagate along the boundary between the matrix and the carbide. The difference in the shape of the carbide at each observation site became slightly prominent around the tempering time of 10 h when SR embrittlement began to appear. Then, the aspect ratio of the particle on the fracture surface is

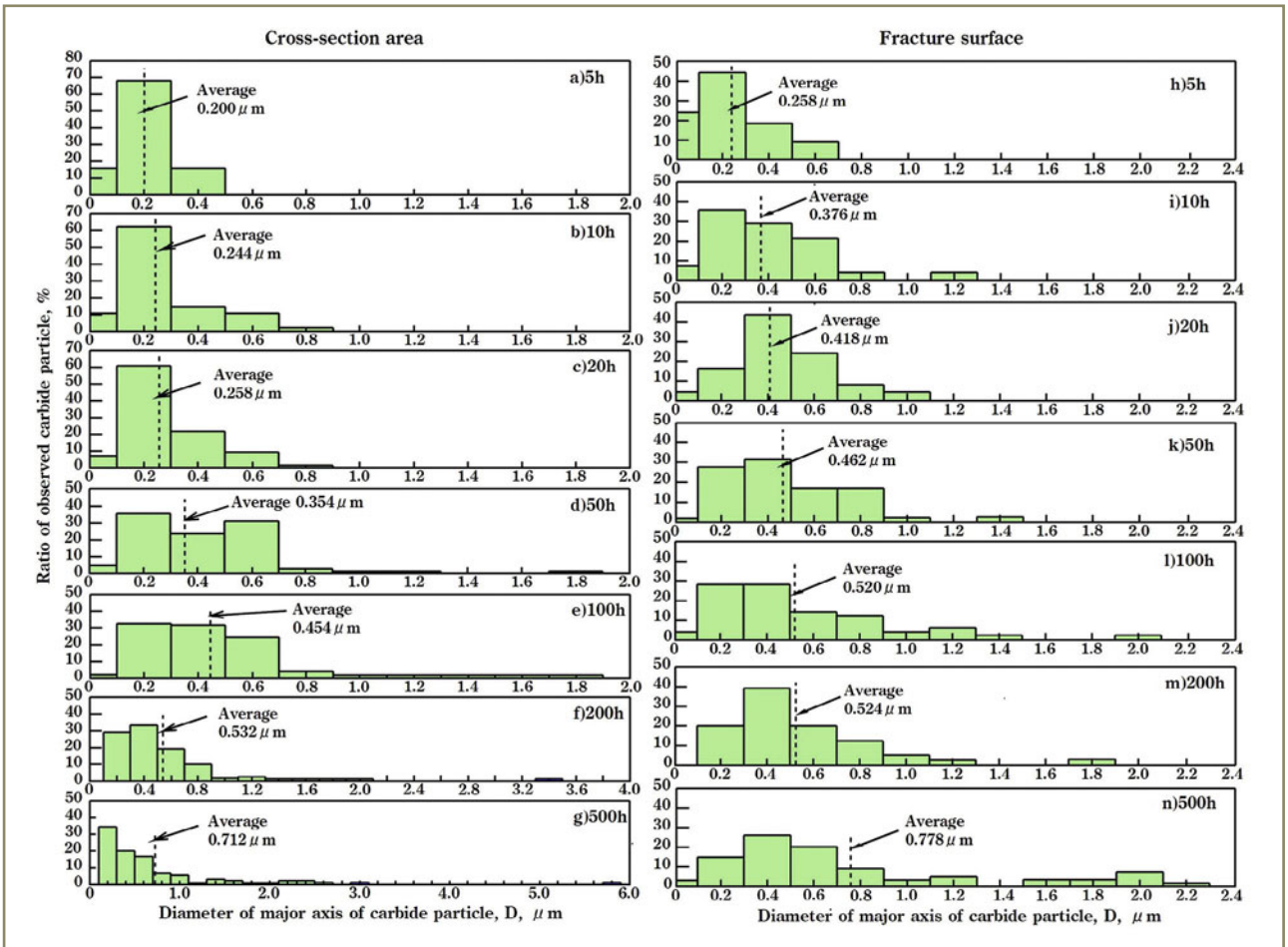

Figure 5 – Distribution of the diameter of the major axis of carbide particle on cross-section area and fracture surface

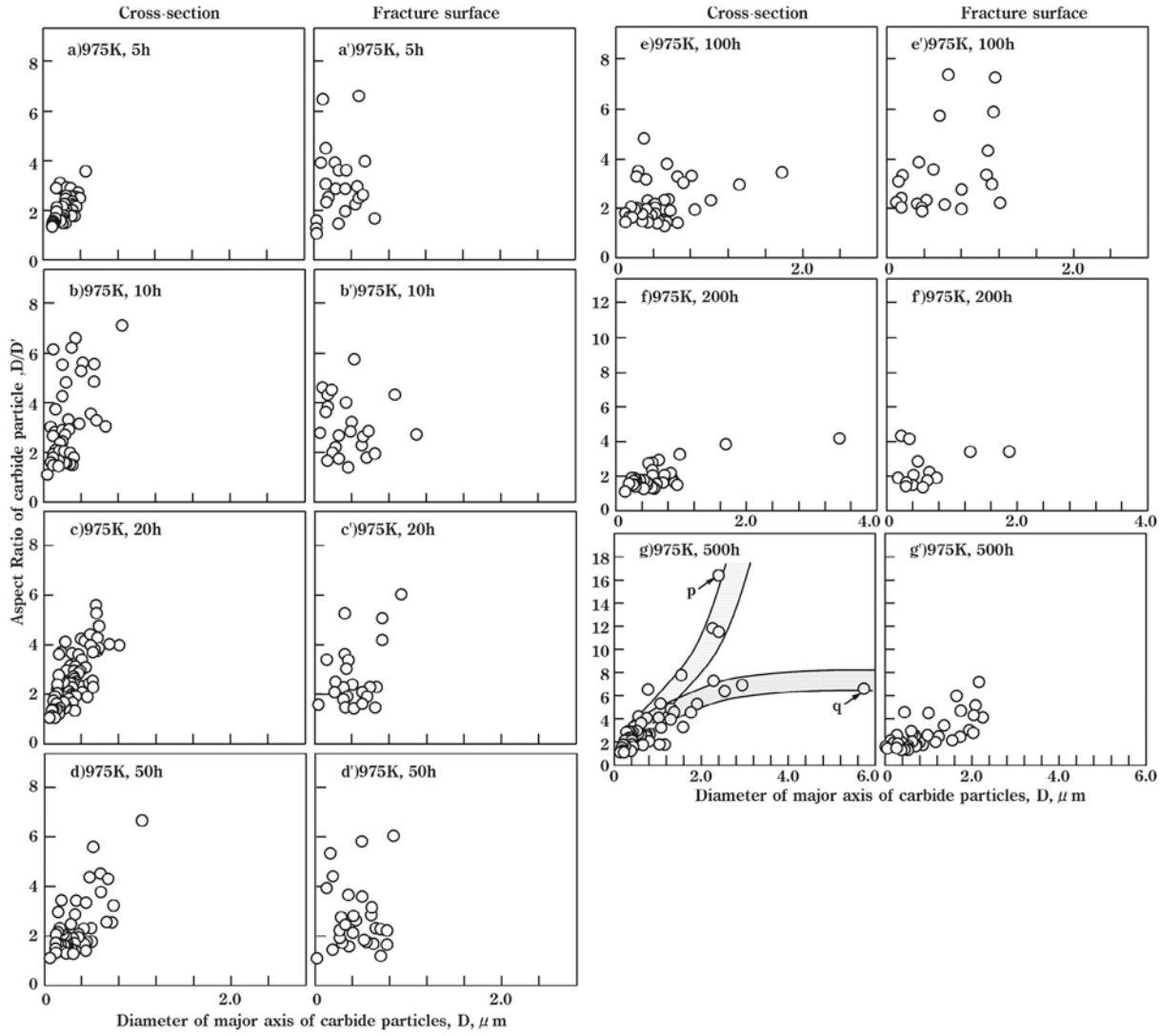

Figure 6 – Comparison between the cross-section and the fracture surface from the viewpoint of the relationship between the aspect ratio and the diameter of the major axis

higher than the particle at the same diameter D in the cross-section area [Figures 6 b) to d) and b') to d')]. On the other hand, the aspect ratio on the fracture surface is lower than that in the cross-section area around 100 h [Figures 6 e), f) and e'), f')]. The carbide particle grew in two ways as types "p" and "q" in the cross-section area [Figure 6 g)]. The former is growth with an increment of the aspect ratio, the latter is growth with an increment of diameter D. These types may correspond with growth of the needle type particle and the polygonal type, respectively. Coarse particles in the cross-section could not be observed on the fracture surface and aspect ratio on the fracture surface is lower than in the cross-section [Figure 6 g')]. These results suggest that the crack may also propagate into the carbide particle.

3.3 SEM observation of coarse carbide particle on the fracture surface

When SR embrittlement appears significantly, the difference in carbide shape was confirmed as shown in Figure 6. The SEM observation result for two pairs of fracture surfaces is shown in Figure 7. The symbols from A to E on the facet P and Q show the past or the present existence positions of a carbide. The holes at position A and C were observed on facet P and the white particle was observed at B in Figure 7 a). However, the hole at B and the particles at A and C were observed in Figure 7 a'). A single particle [ABC] has been broken into three separate particles A, B and C at the fracture surface, with the particles A&C in one of the fracture surfaces and the particle B in the corresponding position on the other surface. This is evidence of the carbide particles also fracturing during embrittlement. On the other hand, three sites with the hole and the particle were observed on facet Q at the position D, E and F in Figures 7 b) and b'). The holes and the particles complement the deficiency for geometric shape on each facet Q. The original shape of each carbide particle is restored by the combination of the particles on both of the fracture surfaces. These photographs show that three original carbides cut along the major axis. Original carbides D and F were polygonal in shape. These carbides may also grow with the combination of the individual carbide particles.

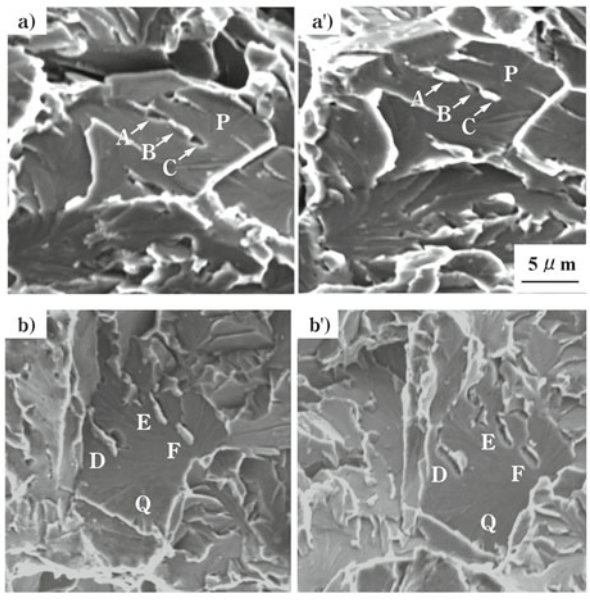

Figure 7 – Carbide particles cut along the minor and major axes of original shape

Crack nucleation is an essential phenomenon when brittle cleavage fracture occurs. Many researchers have investigated the crack nucleation by the microcrack inside the coarsened carbide particle Fe3C in ferritic steel [5-8]. The crack occurred along the minor axis of the particle at a grain boundary which extends linearly to a neighbouring grain boundary [7, 9]. Numerical models to evaluate the cleavage strength σ_c and the transition temperature T_c were already proposed [10, 11]. For example, σ_c and σ_c of Petch's model [11] are given by

$$\sigma_c = \left[\frac{8\mu y_p}{\pi(1-\nu)t} - \frac{k_y d^{1/2}}{8\pi^2 t^2} \right] - \frac{k_y^2 d^{1/2}}{2\sqrt{2}\pi t}$$

$$5.5T_c = 770 + 46.2d^{1/2} - \sigma_c$$

where

μ is the rigidity modulus,

y_p is the effective surface energy,

ν is Poisson's ratio,

t is the carbide thickness,

k_y is the slope in the grain size dependence of the yield stress,

d is total pile-up length.

According to these equations, the increment of the carbide thickness obtains the rise of the transition temperature, i.e. temper embrittlement. Geometric shapes around the notch roots of Charpy impact specimens in the time range when SR embrittlement occurs significantly are shown in Figure 8. Ductile fracture occurs below the notch root because of plastic deformation of the notch. The area of ductile fracture region affects the value of absorbed energy strongly. The facets R&S near the dimple zone correspond to the initiation site of cleavage fracture. The two holes at positions G and H are observed at the edge of facet R like the grain boundary at 200 h [Figure 8 a)]. The crack at carbide/matrix boundary may propagate approximately in a parallel direction along the facet face. This fracture mode resembles that which initiates in the carbide particle at grain boundary in ferritic steel [7]. In the case of 500 h, the facet S corresponds to the crack initiation site, because the crack from the facet S propagates to the facet T which was formed along the macrocrack direction [Figure 8 b)]. The morphology of the carbide particles at the centre of the facet S is shown in Figure 9. Each particle and hole at positions I, J and K on both of the fracture surfaces complement the deficiency for geometric shape, the same as for the facets P and Q in Figure 7. These observation results suggest that each crack at the carbide matrix boundary and inside the carbide particle affects the initiation of cleavage fracture.

3.4 X-ray diffraction test and TEM observation of coarse carbide

The X-ray diffraction test and TEM observation were executed to identify the coarse carbide particles. Figure 10

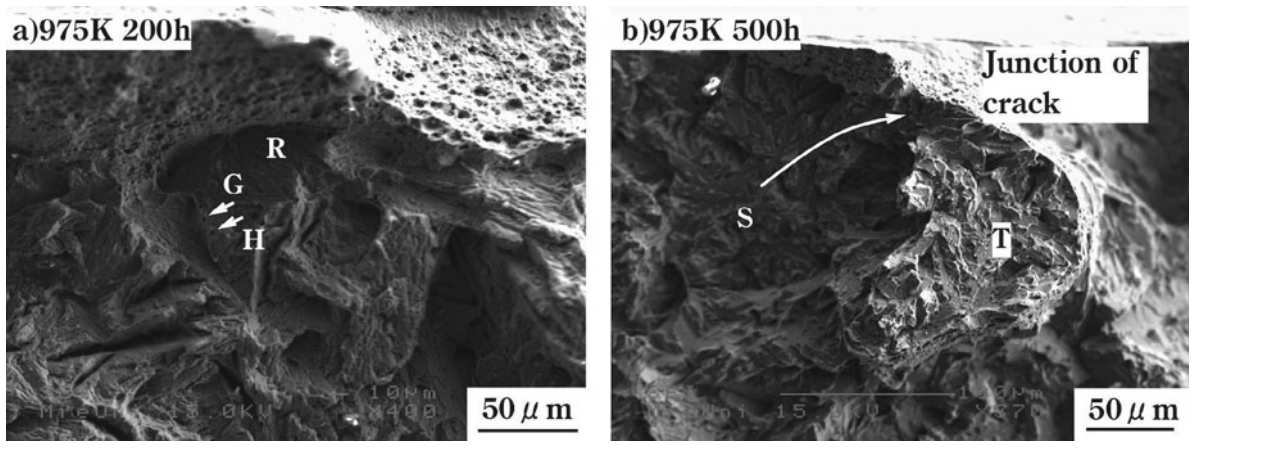

Figure 8 – Facets R and S at the initiation region of cleavage fracture

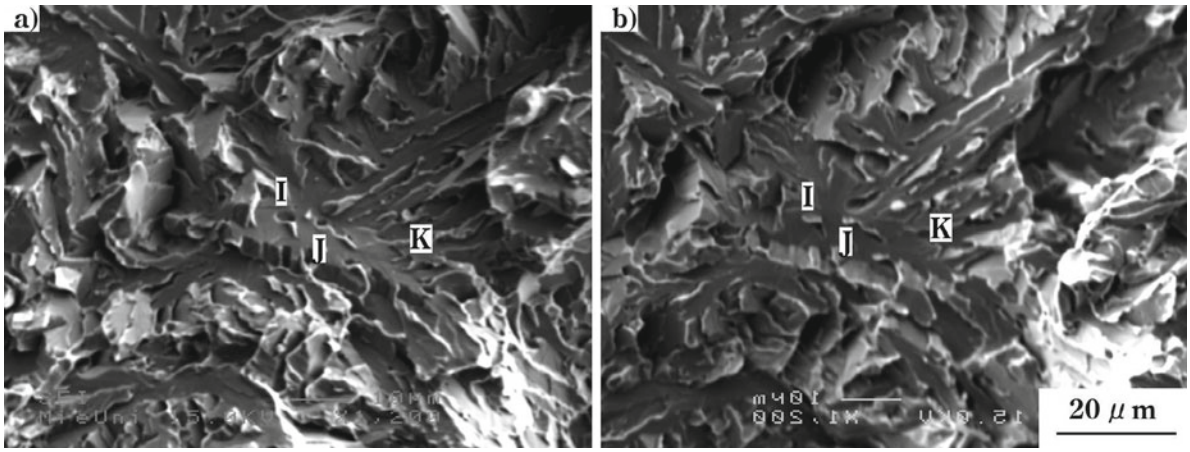

Figure 9 – Broken carbide particles at the crack initiation facet S, as shown in Figure 8 b)

shows the result of the X-ray diffraction test for the type of the carbide precipitated at SR temperature. The carbide was obtained by electrolytic extraction [12]. M_3C, M_2C, M_7C_3 and $M_{23}C_6$ carbides have a diffraction spectrum of Fe_3C, Mo_2C, Cr_7C_3 and $Cr_{23}C_6$, respectively. M_7C_3, $M_{23}C_6$ and M_2C precipitated at the SR embrittlement region. The change in the order of relative amount ratio could not be confirmed in this experiment condition. The result of the X-ray diffraction test narrows down the type of coarse carbide particle.

Figure 11 shows the bright field image and the electron diffraction pattern of the coarse carbide by TEM observation. The specimen for TEM observation was prepared by electrical polishing [13]. The coarse carbide particle was identified as $M_{23}C_6$ from this result.

4 Discussion

The effect of the coarse carbide particle on SR embrittlement is considered by the calculation results based on the Eshelby theory [14], with the assumption that the crack propagates and fracture occurs under the local uniaxial tensile loading condition. The mechanical properties of the matrix (steel) and $M_{23}C_6$ ($Cr_{23}C_6$) carbide are shown in Table 2.

4.1 Diameter dependency of plastic strain for decohesion at carbide/matrix boundary

Plastic strain is obtained by the following equation from the energy criterion for decohesion of the sphere carbide from the matrix [16].

$$\varepsilon_{crit} = \beta\left(\frac{E}{E^* d}\right)^{\frac{1}{2}}$$

where

$$\alpha = \frac{E^*}{E}$$

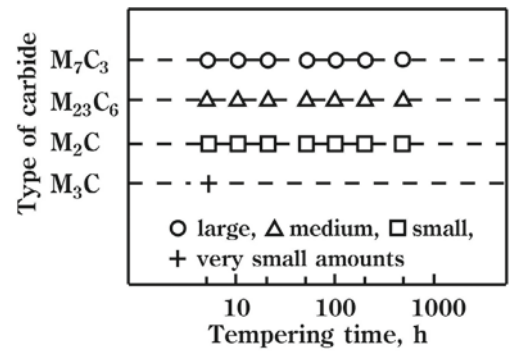

Figure 10 – Result for the type of carbide by X-ray diffraction test

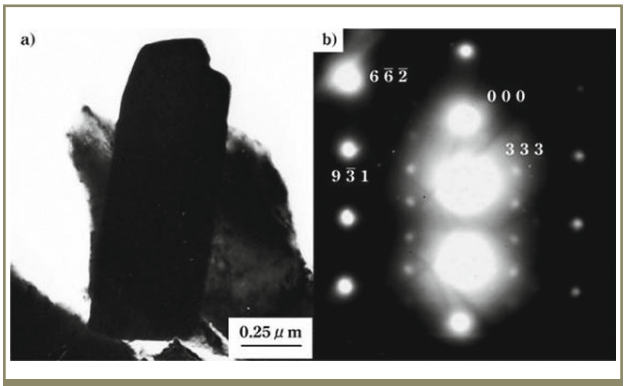

Figure 11 – Bright field image and electron diffraction pattern of coarse carbide particle

Table 2 – Young's modulus, Poisson's ratio, coefficient of thermal expansion of steel and $Cr_{23}C_6$ for calculation

Steel	E [GPa]	210
	ν	0.3
	CTE [10^{-6}/K]	12
$Cr_{23}C_6$	E^* [GPa]	357
	ν^*	0.3
	CTE* [10^{-6}/K]	10
E^* and ν^* are quoted from reference [15].		

$$\beta^2 = \frac{48\times10^{-9}\left\{(7-5\nu)(1+\nu^*)+(1+\nu)(8-10\nu)\alpha\right\}\times\left\{(7-5\nu)(1-\nu^*)+5(1-\nu^2)\alpha\right\}}{(7-5\nu)^2\left\{2(1-2\nu^*)+(1+\nu)\alpha\right\}}$$

d is the diameter of the sphere particle and

E, E^*, ν and ν^* are Young's modulus and Poisson's ratio of the matrix and the carbide, respectively. Figure 12 shows diameter dependency of plastic strain for decohesion at the carbide/matrix boundary. In case of fine carbide, decohesion of the carbide from the matrix requires large plastic strain. Fine carbide particles observed at the de-embrittled state may resist the crack propagation along the carbide/matrix boundary when brittle cleavage fracture with small strain occurs. In the case of coarse carbide, decohesion at the boundary requires very small plastic strain. The crack of brittle fracture propagates easily along the coarse carbide/matrix boundary.

4.2 Aspect ratio dependency of strain by internal stress

The dependency of strain which occurred in the carbide and matrix/carbide boundaries by internal stress on aspect ratio during the low temperature impact test is evaluated in this section. Oblate spheroidal carbide particle can be represented by following equation.

$$\frac{x^2}{a^2}+\frac{y^2}{a^2}+\frac{z^2}{c^2}=1 \qquad 0\le c/a\le 1$$

Moreover, internal stress σ_{total} is obtained by following equation.

$$\sigma_{total}=\sigma_{mis}+\sigma_{inh}+\sigma_{p}$$

σ_{mis}, σ_{inh} and σ_{p} are internal stresses by thermal expansion, elastic modulus and plastic deformation effect. Each internal stress can be calculated with eigen strain and Eshelby tensor [17]. σ_{mis} was calculated with temperature deference between SR treatment and the impact test of 900 K. σ_{inh} was calculated as 100 Mpa referred the yield stress of temper-embrittled steel at low temperature [18]. σ_{p} was calculated with the plastic strain at the matrix of 0.001 %. Comparison of aspect ratio dependency in the carbide and that at the carbide/matrix boundary is shown in Figure 13. In the case of low aspect ratio carbide, plastic strain by internal stress at the carbide/matrix boundary is larger than that in the carbide. The crack may propagate along the carbide/matrix boundary easily, because plastic strain introduced by internal stress promotes decohesion at the carbide/matrix boundary. Increment of aspect ratio decreases plastic strain by internal stress. In the case of high aspect ratio carbide, plastic strain at the carbide/matrix boundary resembles that in the carbide. The crack propagation site may not be only the carbide/matrix boundary, but also the carbide.

Discussion in this section can be summarized as follows. The crack propagates along the carbide/matrix boundary easily with increment of the diameter of the carbide particle. Therefore, increment of density of the carbide particle observed on the fracture surface, as compared with the cross-section area, can occur as shown in Figure 4 c). The crack propagates easily into the coarse carbide particle with a high aspect ratio. Then, the segments of the carbide particles can be observed on the fracture surface as shown in Figure 7.

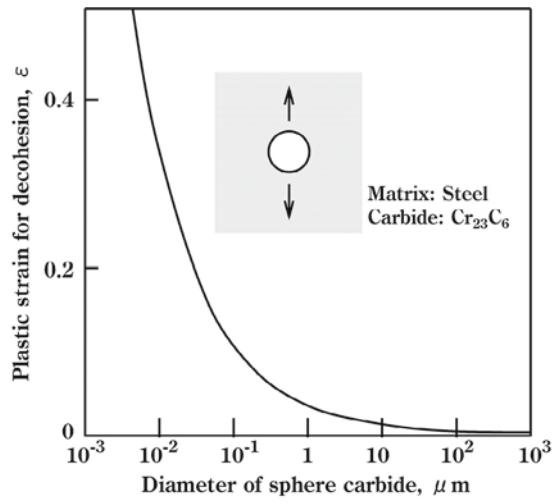

Figure 12 – Diameter dependency of plastic strain for decohesion at the carbide/matrix boundary

5 Conclusion

Image processing was developed to evaluate the shapes of the carbide particles in the SEM image. It was applied to the carbide particles in HAZ of 2 1/4Cr-1Mo steel which

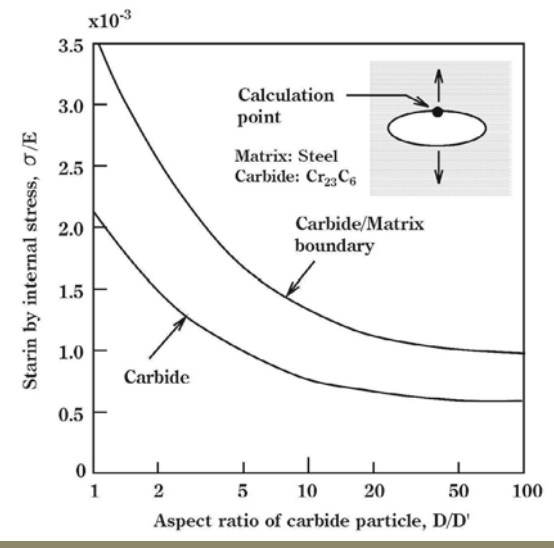

Figure 13 – Aspect ratio dependency for strain by internal stress

were tempered at stress relief annealing temperature. The carbide particle grows along one direction, mainly with progress of SR treatment. However, when SR embrittlement occurs significantly, some coarse polygonal particle can also be observed in the cross-section area. Coarse particles on the facet of cleavage fracture were cut along major and minor axes. The same broken carbide particles were also observed at the initiation facet of cleavage fracture. Coarse carbide particles may promote SR embrittlement by crack propagation and crack initiation at the carbide/matrix boundary and inside the carbide.

References

[1] Kawakami H., Tamaki K., Suzuki J. and Ichikawa Y.: Temper embrittlement in the HAZ of 2 1/4Cr-1Mo steel induced by reheating after SR treatment, Welding International, 1999, vol. 13, no. 2, pp. 19-27.

[2] Tamaki K., Kawakami H. and Suzuki J.: Temper embrittlement in HAZ of Cr-Mo Steel, Doc. IIW-1425-98, Welding in the World, 1999, vol. 43, no. 2, pp. 36-48.

[3] Tamaki K., Kawakami H., Suzuki J. and Niinomi T.: Temper embrittlement in HAZ of Cr-Mo steels arising in the temperature range of SR treatment, Quarterly Journal of the Japan Welding Society, 1997, vol. 15, no. 3, pp. 502-508 (in Japanese).

[4] Tamaki K., Kawakami H., Suzuki J., Kojima M. and Niinomi T.: Temper embrittlement in HAZ of Cr-Mo steels arising in temperature range of stress relieving, 1996, IIW Doc. IX-1834-96, pp. 1-24.

[5] Hahn G.T.: The influence of microstructure on brittle fracture toughness, Metallurgical Transaction A, 1984, vol. 15, no. 6, pp. 947-959.

[6] Beremin F.M.: A local criterion for cleavage fracture of a nuclear pressure vessel steel, Metallurgical Transaction A, 1983, vol.14, no. 11, pp. 2277-2287.

[7] Lin T., Evans A.G. and Ritchie R.O.: Stochastic modeling of the independent roles of particle size and grain size in transgranular cleavage fracture, Metallurgical Transaction A, 1987, vol. 18, no. 4, pp. 641-651.

[8] Thompson A.W. and Knott J.F.: Micromechanisms of brittle fracture, Metallurgical Transaction A, 1993, vol. 24, no. 3, pp. 523-534.

[9] Curry D.A. and Knott J.F.: Effects of microstructure on cleavage fracture stress in steel, Metal Science, 1978, vol. 12, no. 11, pp. 511-514.

[10] Minz B., Morrison W.B. and Cochrane R.C.: Advances in Physical Metallurgy and Applications of Steel, Proceedings of Conference, University of Liverpool, Liverpool, Sept. 1981, TMS, Warrendale, PA, 1982, pp. 222-228.

[11] Petch N.J.: The Influence of grain boundary carbide and grain size on the cleavage strength and impact transition temperature of steel, Acta Metallurgica, 1986, vol. 34, no. 7, pp. 1387-1393.

[12] Tamaki K., Suzuki J. and Nakaseko Y.: Influence of carbides on the reheat cracking, Journal of the JWS, 1983, vol. 52, no. 2, pp. 131-140 (in Japanese).

[13] Miyata K., Omura T., Kushida T. and Komizo Y.: Coarsening kinetics of multicomponent MC-type carbides in high-strength low-alloy steels, Metallurgical and Materials Transactions A, 2003, vol. 34, no. 8, pp. 1565-1573.

[14] Eshelby J.D.: The determination of the elastic field of an ellipsoidal inclusion, and related problems, Proceedings of the Royal Society of London, Series A, Mathematical and Physical Sciences, 1957, vol. 241, no. 1226, pp. 376-396.

[15] Jiang C.: First-principles study of structure, elastic, and electron properties of chromium carbides, Applied Physics Letters, 2008, vol. 92, no. 4, pp. 1-3.

[16] Tanaka K., Mori T. and Nakamura T.: Cavity formation at the interface of a spherical inclusion in a plastically deformed matrix, Philosophical Magazine, 1970, vol. 21, no. 170, pp. 267-279.

[17] Shibata M. and Ono K.: Internal stress due to an oblate spheroidal inclusion: Misfit, inhomogeneity and plastic deformation effect, Acta Metallurgica, 1978, vol. 26, no. 6, pp. 921-932.

[18] Sakui S., Nakamura T. and Ohmori M.: Impact tensile test of temper embrittlement steels at low temperature, Tetsu-to-Hagane, 1963, vol. 49, no. 3, pp. 544-545 (in Japanese).

About the authors

Dr. Eng. Hiroshi KAWAKAMI (kawakami@mach.mie-u.ac.jp), Prof. Emeritus Koreaki TAMAKI (tamaki@met.mach.mie-u.ac.jp), Prof. Jippei SUZUKI (jsuzuki@mach.mie-u.ac.jp), Mr. Kanta TAKAHASHI (takahasi@met.mach.mie-u.ac.jp), Mr. Yousuke IMAE (imae@met.mach.mie-u.ac.jp) and Mr. Soichiro OGUSU (ogusu@met.mach.mie-u.ac.jp) are all with Graduate School of Engineering, Mie University, Mie (Japan).